Electrochemical genoassays on gold-coated magnetic nanoparticles to quantify genetically modified organisms (GMOs) in food and feed as GMO percentage

Alexandra Plácido[a], Clara Pereira[b], Alexandra Guedes[c], M. Fátima Barroso[a], Rebeca Miranda-Castro[d], Noemí de-los-Santos-Álvarez[d], , Cristina Delerue-Matos[a]

[a] *REQUIMTE/LAQV, Instituto Superior de Engenharia do Porto, Instituto Politécnico do Porto, Rua Dr. António Bernardino de Almeida, 431, 4200-072 Porto, Portugal*
[b] *REQUIMTE/LAQV, Departamento de Química e Bioquímica, Faculdade de Ciências, Universidade do Porto, Rua do Campo Alegre s/n, 4169-007 Porto, Portugal*
[c] *Centro de Geologia e Departamento de Geociências, Ambiente e Ordenamento do Território, Faculdade de Ciências, Universidade do Porto, Rua do Campo Alegre s/n, 4169-007 Porto, Portugal*
[d] Departamento de Química Física y Analítica, Av. Julián Clavería 8, 33006 Oviedo, Spain

A B S T R A C T

The integration of nanomaterials in the field of (bio)sensors has allowed developing strategies with improved analytical performance. In this work, ultrasmall core-shell Fe_3O_4@Au magnetic nanoparticles (MNPs) were used as the platform for the immobilization of event-specific Roundup Ready (RR) soybean and taxon-specific DNA sequences. Firstly, monodisperse Fe_3O_4 MNPs were synthesized by thermal decomposition and subsequently coated with a gold shell through reduction of Au(III) precursor on the surface of the MNPs in the presence of an organic capping agent. This nanosupport exhibited high colloidal stability, average particle size of 10.2 ± 1.3 nm, and spherical shape. The covalent immobilization of ssDNA probe onto the Au shell of the Fe_3O_4@Au MNPs was achieved through a self-assembled monolayer (SAM) created from mixtures of alkane thiols (6-mercapto-1-hexanol and mercaptohexanoic acid). The influence of the thiols ratio on the electrochemical performance of the resulting electrochemical genoassays was studied, and remarkably, the best analytical performance was achieved for a pure mercaptohexanoic acid SAM. Two quantification assays were designed; one targeting an RR sequence and a second targeting a reference soybean gene, both with a sandwich format for hybridization, signaling probes labelled with fluorescein isothiocyanate (FITC), enzymatic amplification and chronoamperometric detection at screen-printed carbon electrodes (SPCE). The magnetogenoassays exhibited linear ranges from 0.1 to 10.0 nM and from 0.1 to 5.0 nM with similar detection limits of 0.02 nM and 0.05 nM for the event-specific (RR) and the taxon-specific (lectin) targets, respectively. The usefulness of the approach was demonstrated by its application to detect genetically modified organisms (GMOs) in feed and food.

Keywords:
Core-shell Fe_3O_4@Au magnetic nanoparticles
GTS 40-3-2
Electrochemical genoassay
Genetically modified soybean
GMO quantification

1. Introduction

The insertion of new characteristics, like agronomic/technological improvements, in plants and organisms by genetic engineering has revolutionized modern agriculture and contributed to food security, sustainability and climate change. Over the last 21 years of commercialization, the global area of biotech crops has increased 110-fold, achieving 185.1 million hectares in 2016. Soybean (*Glycine max* L.) remains the most important genetically modified (GM) crop with about 111 million hectares of planted area, which corresponds to 83% of the global area of biotech crops (ISAAA, 2016). Thus, soybean is a very relevant crop in the global food industry, being an ingredient widely used in many foodstuffs worldwide.

The introduction of genetically modified organisms (GMOs) in the food chain has generated an intense public and scientific debate about their risks and the need to provide information to the consumer. In the European Union (EU), all transgenic crops need authorization prior to entering the market. On a regulation basis the labelling of food products containing GM material is mandatory unless its content is no higher than 0.9% provided that the presence is adventitious or technically unavoidable (European Commission, 2003). In order to ensure the implementation of legislation, it is necessary to adopt methodologies that allow assessing food quality and quantifying GMOs.

DNA-based techniques are the methods of choice for GMO detection

due to their ability to detect the foreign piece of DNA inserted, that is, the actual analyte. Real-time PCR is currently considered the gold standard and the reference method for GMO testing due to their high specificity, sensitivity and reliability. However, new approaches using biosensor platforms, especially those that use electrochemical detection, are currently a promising strategy due to their low cost, easy monitoring, and automatic on-line and portable options. In this sense, the development of genoassay/genosensor methods based on the amplification of a specific DNA sequence and its subsequent hybridization with complementary probes is a good alternative to the reference method to test the veracity of the labelling and hence the authenticity of foodstuffs. Great progress has been achieved in the platforms of electrochemical DNA sensing (Arugula et al., 2013; Kamle and Ali, 2013; Plácido et al., 2016). These approaches cover three stages of GMO testing: (i) screening methods (promoters and terminators), (ii) gene-specific methods, and (iii) event-specific methods. The two former only allow to ascertain the presence or absence of the GMOs, as a preliminary analysis, while only the latter is able to provide unambiguous evidence of the specific event and thus quantify it.

Relative quantification of GMOs, that is, strategies aimed at two reactions, one targeting the taxon-specific gene and the other targeting the event-specific sequence, performed on the same DNA template is compulsory to verify that the legislation is being complied. However, only recently it has been reported in combination with bioassays (Manzanares-Palenzuela et al., 2015) making previous approaches useless for that purpose.

Core-shell gold-coated iron oxide magnetic nanoparticles (Fe_xO_y@Au MNPs) have been attracting considerable interest in the bioassays field owing to their superparamagnetic properties and easy functionalization of the gold shell with thiolated molecules leading to the formation of a self-assembled monolayer (SAM), which renders an organized and stable surface amenable to readily attached biomolecules (Freitas et al., 2016). It is well-known that efficient genosensor performance requires an optimized amount of capture DNA probe. This is usually achieved with a second thiol, typically 6-mercapto-1-hexanol (MCH). Using a third thiol (specifically a dithiol) (Wu et al., 2010) or a thioaromatic thiol (Moura-Melo et al., 2015) resulted in highly improved signal-to-blank ratio, decreasing the limit of detection of genosensors. Beyond direct immobilization of a thiolated DNA probe, covalent linkage to an appropriate thiolated spacer also showed advantages in terms of low background currents (Miranda-Castro et al., 2017).

In this work, monodisperse superparamagnetic core-shell Fe_3O_4@Au MNPs were synthesized, functionalized with a SAM containing MCH and MCHac (mercaptohexanoic acid) and used as the platform for an electrochemical genoassay. The magnetic cores (Fe_3O_4) were synthesized by thermal decomposition of the organometallic precursor iron(III) acetylacetonate, [Fe(acac)$_3$], in a high-boiling point solvent (1-methyl-2-pyrrolidinone) in the presence of surfactants (oleic acid and oleylamine) that stabilized and prevented the agglomeration between the MNPs. This chemical process allowed obtaining MNPs with uniform and tunable sizes and morphology control. The surface coating of the Fe_3O_4 nanoparticles with a gold shell by reduction of Au(III) to Au(0), under controlled conditions, was performed to prevent the oxidation of the Fe_3O_4 MNPs and their aggregation, to control the Au shell thickness and to provide the immobilization layer to DNA through Au-S bonding. The magnetic properties of this platform facilitate the washing steps during the genoassay procedure, avoiding non-specific adsorptions (Paleček and Fojta, 2007). The nanobiointerface design is crucial in the bioassay/sensor performance and its formation and properties depend on several factors, like effective surface area, surface charge, and functional groups. Thus, their composition was optimized along with the surface-to-volume ratio of the NPs used in their formation. The nanostructures were characterized by transmission electron microscopy (TEM), energy dispersive X-ray spectroscopy (EDX), UV–vis spectroscopy, X-ray diffraction, Raman spectroscopy and sulphur elemental analysis to study their morphology, particle size, structure and chemical composition.

For GMO testing two measurements were performed, one targeting a DNA fragment from the insertion point of the transgenic construct of Roundup Ready (RR) soybean, an event-specific sequence, and a second targeting a fragment of the taxon-specific soybean gene, *lectin*. The proposed approach showed the adequate sensitivity and selectivity to be successfully applied to real samples quantified as a GMO percentage.

2. Experimental section

2.1. Reagents

1-hexadecanol (95%), 1-methyl-2-pyrrolidinone (NMP, ≥ 99.0%), oleic acid (90%), anhydrous toluene (99.8%), 6-mercapto-1-hexanol, 6-mercaptohexanoic acid (90%), 4-(2-hydroxyethyl)piperazine-1-ethanesulfonic acid (HEPES, ≥ 99.5%), concentrated saline sodium phosphate-EDTA (20× SSPE, pH 7.4), *N*-(3-dimethylaminopropyl)-*N*′-ethylcarbodiimide hydrochloride (EDC), *N*-hydroxysuccinimide (NHS), ethanolamine (≥ 99.0%), albumin from bovine serum (BSA, > 99%), 3,3′,5,5′-tetramethylbenzidine (TMB, Neogen K-blue enhanced activity substrate containing H_2O_2) were purchased from Sigma-Aldrich. Iron (III) acetylacetonate ([Fe(acac)$_3$], > 99%), and oleylamine (80–90%) were obtained from Acros Organics. Hydrogen tetrachloroaurate(III) trihydrate ($HAuCl_4 \cdot 3H_2O$, 99.99%, ≥ 49.0% Au basis) was supplied by Alfa Aesar. Panreac provided sodium chloride (NaCl, 99.5%), and Tween 20 was received from Merck. Casein 1% (w/v) blocking solution in 1× phosphate buffer saline (PBS) and absolute ethanol (analytical grade) were purchased from Thermo Scientific. Antifluorescein-peroxidase (antiFITC-POD) Fab fragments were obtained from Roche Diagnostics GmbH (Mannheim, Germany). All commercially available reagents were used without further purification. Throughout this work, the solutions were prepared using Milli-Q water (specific resistivity 18.2 MΩ cm), obtained from a Millipore (Simplicity 185) water purification system.

Different buffers were used in the experiments: (i) immobilization buffer: HEPES (0.1 M, pH 7.4); (ii) hybridization buffer: SSPE (2× SSPE, pH 7.4); (iii) washing buffers: HEPES-T (0.1 M HEPES, 0.01% Tween 20); SSPE-T (2× SSPE, 0.01% Tween 20); and (iv) conjugate buffer: PBS-C (1× PBS solution containing 1% casein).

Desalted synthetic DNA oligonucleotides (probes and target sequences) were purchased from Sigma-Aldrich, and primers were synthesized by Metabion International AG (Planegg, Germany). Their sequences are listed in Table S1. All stock solutions were prepared in Milli-Q water and stored at −20 °C.

2.2. Synthesis of magnetic nanomaterial, genoassay procedure and instrumentation

The detailed protocols and equipment used are described in Supporting information.

3. Results and discussion

3.1. Morphologic, structural, and chemical characterization of Fe_3O_4, Fe_3O_4@Au, and functionalized Fe_3O_4@Au MNPs

In order to confirm the successful preparation of the Fe_3O_4@Au MNPs, the parent and gold-coated Fe_3O_4 MNPs were characterized by TEM and UV–vis spectroscopy.

The TEM micrographs, the particle size distribution histograms and EDX analysis of Fe_3O_4 and Fe_3O_4@Au are presented in Fig. 1. The TEM image of Fe_3O_4 shows nanometer-sized particles (4.2 ± 0.6 nm) with a spherical shape and a Gaussian-type size distribution (Fig. 1A and B). The presence of iron and oxygen in the sample was confirmed by EDX spectroscopy (Fig. 1C) (Robinson et al., 2010). Similarly Fe_3O_4@Au

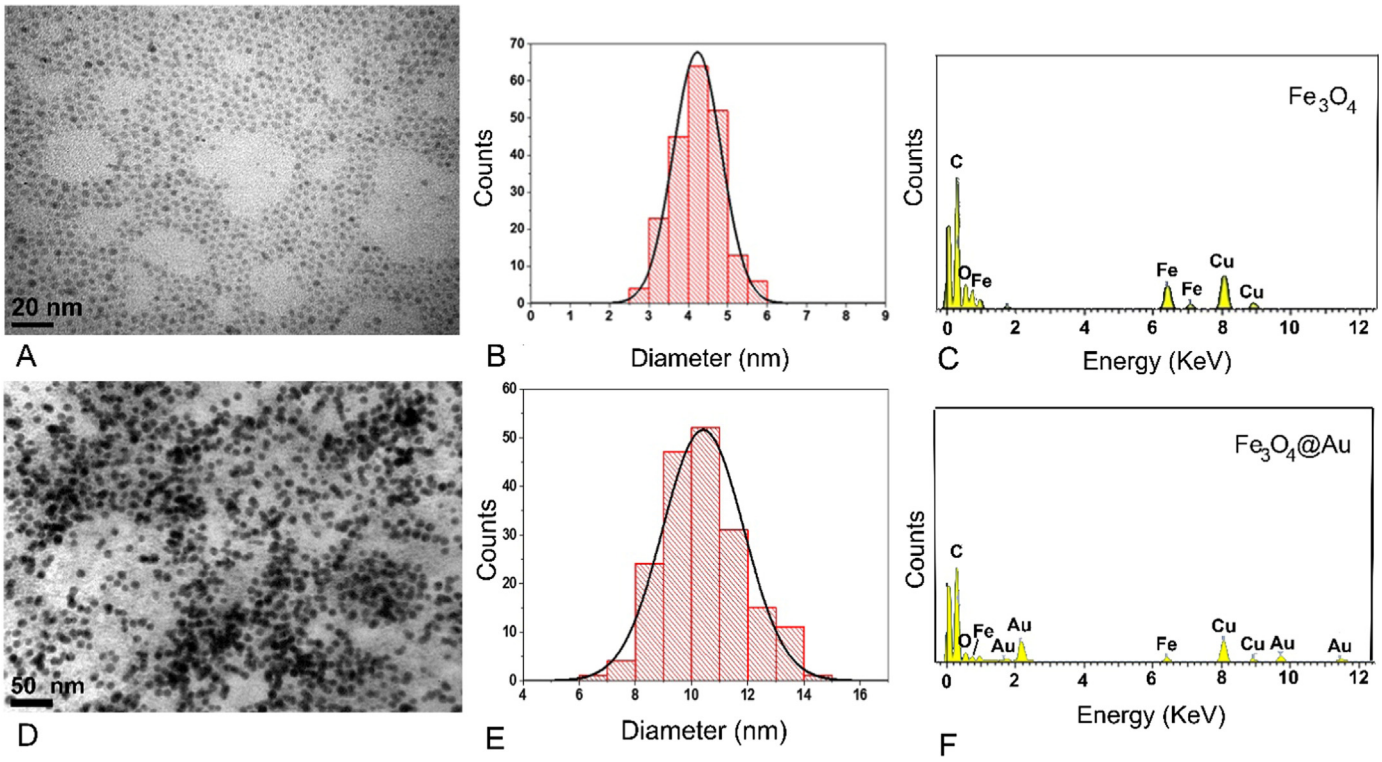

Fig. 1. TEM micrographs and particle size distribution histograms of (A), (B) Fe_3O_4, and (D), (E) Fe_3O_4@Au MNPs (the solid curves represent the particle size distribution fittings). EDX spectra of the (C) Fe_3O_4, and (F) Fe_3O_4@Au MNPs. The presence of carbon and copper is due to the grid used for the TEM/EDX experiments.

MNPs presented spherical shape with a darker contrast and a Gaussian-type particle size distribution (Fig. 1D and E). The average size increased to 10.2 ± 1.3 nm, as expected. Furthermore, they were well-dispersed with no signs of aggregation, confirming the successful coating of the MNPs yielding core-shell structures, as seen previously (Freitas et al., 2016; Xu et al., 2007). EDX results confirmed the presence of gold (Fig. 1F). The observed decrease of the intensity of the Fe and O peaks indicates that the Fe_3O_4 cores were successfully coated.

Fig. S1 shows the UV–vis absorption spectra of the colloidal dispersions of Fe_3O_4 and Fe_3O_4@Au. As expected, the surface plasmon resonance (SPR) band at $\lambda = 529$ nm was only observed with Fe_3O_4@Au MNPs, resulting from the oscillation frequency characteristic of plasmon resonance in the gold surface (Boisselier and Astruc, 2009). In fact, Boisselier et al. reported that 5 nm diameter spherical gold nanoparticles dispersed in ethanol have their SPR band at 520 nm (Boisselier and Astruc, 2009). Since the average size of the Fe_3O_4@Au MNPs prepared in this work is 10.2 nm and considering that the magnetic cores size is 4.2 nm, the gold shell thickness is ~ 6.0 nm, which is larger than the Au particle size reported by Boisselier et al., which can explain the appearance of the SPR band at a higher wavelength. These results confirm the successful formation of core@shell gold-coated Fe_3O_4 MNPs, in accordance with TEM.

XRD technique was also used to confirm the crystallinity, composition and estimate the particle size of the nanomaterials. The diffractograms of the Fe_3O_4 and Fe_3O_4@Au MNPs are shown in Fig. 2. In the XRD pattern of Fe_3O_4 MNPs are detected eight diffraction peaks at $2\theta = 18.6°$, 30.6°, 35.5°, 43.1°, 53.5°, 57.2°, 62.5° and 74.0° which are assigned to the (111), (220), (311), (400), (422), (511), (440) and (533) Bragg reflections of ferrites with a cubic spinel structure (*Fd*3*m* space group) (Freitas et al., 2016; Wang et al., 2005, 2013). The lattice parameter *a* of the cubic unit cell was determined, being 8.382 Å, which is close to the *a* value for bulk Fe_3O_4 (a = 8.396 Å, JCPDS card 19-0629), revealing that magnetite is the main type of iron oxide present in the sample. The observed diffraction peak broadening is due to the small size of the ferrite nanoparticles.

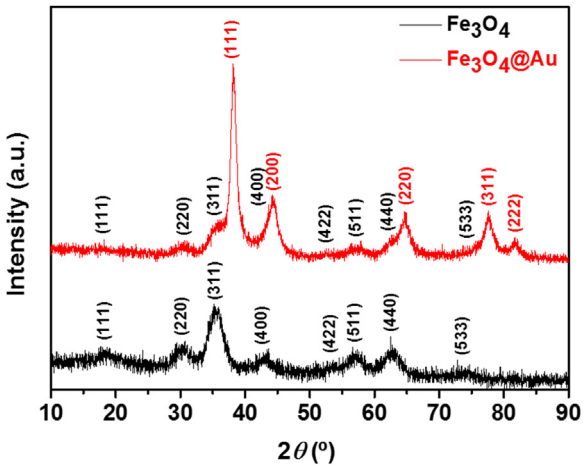

Fig. 2. X-ray diffractograms of Fe_3O_4 and Fe_3O_4@Au samples.

In the case of Fe_3O_4@Au sample, the diffractogram showed additional diffraction peaks at $2\theta = 38.2°$, 44.2°, 64.7°, 77.6° and 81.7° (highlighted in red), which can be indexed to (111), (200), (220), (311) and (222) planes of gold with a cubic structure (*Fm*3*m* space group, JCPDS card 04-0784) (Freitas et al., 2016; Robinson et al., 2010; Wang et al., 2013). Furthermore, the Bragg reflections associated with the Fe_3O_4 cores are weaker, because of the gold coating encapsulating Fe_3O_4. These results confirm the successful coating of the MNP cores, corroborating the TEM and UV–vis spectroscopy results. Finally, the diffraction peaks of gold were more intense than those reported by Freitas et al. for Fe_3O_4@Au MNPs prepared using a Fe_3O_4:Au precursor ratio of 1:4 (Freitas et al., 2016), which is due to the larger thickness of the gold shell since in this work a lower Fe_3O_4:Au ratio was used (1:7 *vs.* 1:4), resulting in core-shell MNPs with slightly larger size (10.2 vs.

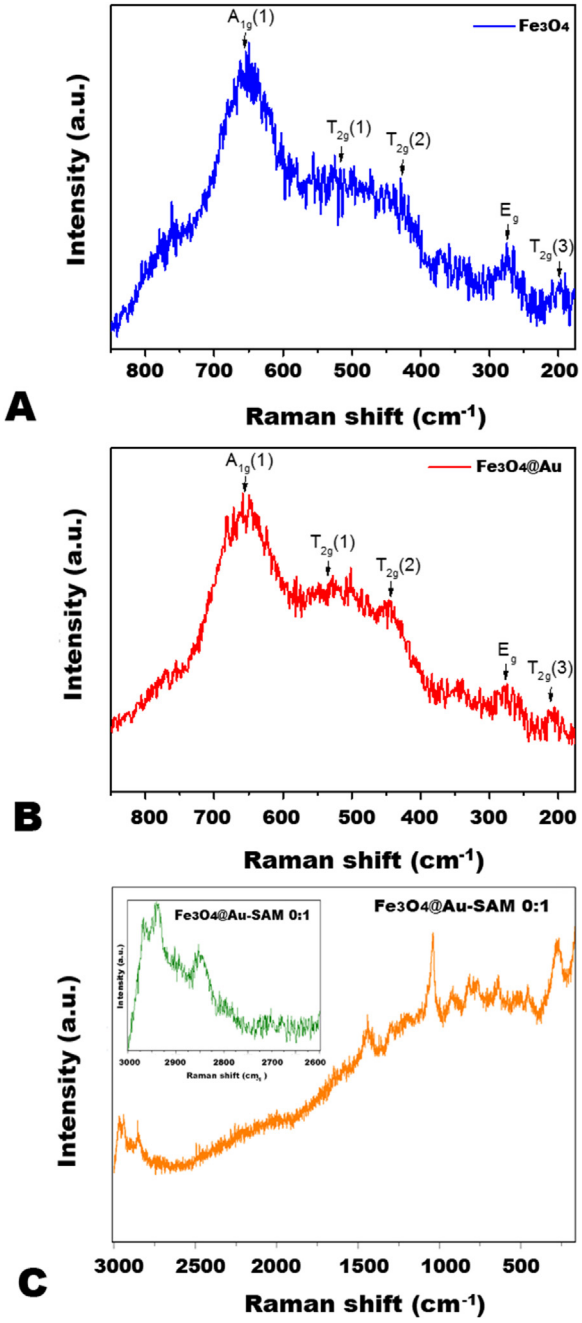

Fig. 3. Raman spectra of (A) Fe_3O_4 and (B) Fe_3O_4@Au in the 850–175 cm^{-1} range, and of (C) Fe_3O_4@Au-SAM functionalized with SAM MCH:MCHac 0:1 in the 3000–150 cm^{-1} range (Inset: magnified view of Fe_3O_4@Au-SAM 0:1 Raman spectra in the 3000–2600 cm^{-1} range).

10.0 nm).

The average crystallite size of the parent Fe_3O_4 MNPs was calculated using the Debye-Scherrer equation (Dinnebier and Billinge, 2008), from the full width at half-maximum (fwhm) of the (311) reflection peak. The value found was 3.4 nm, which is close to the value obtained by TEM (4.2 ± 0.6 nm). For Fe_3O_4@Au MNPs it was not possible to determine the diameter of the cores after the gold coating because of the partial overlapping of the (111) and (311) reflection peaks of gold and magnetite, respectively.

To provide further insights on the chemical composition of the magnetic nanosupports, the parent Fe_3O_4 MNPs before and after the coating with the gold shell and functionalization with SAMs were characterized by Raman spectroscopy. As can be seen in Fig. 3, the Raman spectra of the samples exhibit broad peaks due to the small size of the nanoparticles (Kolen'ko et al., 2014). In order to make a more precise analysis of the active vibrational modes in Raman, a deconvolution of the Raman spectra of the samples was carried out (Fig. S2). For both Fe_3O_4 and Fe_3O_4@Au materials, the five phonon modes characteristic of ferrites with a cubic spinel structure (*Fd3m* crystal space group) are observed: A_{1g} (656 cm^{-1}), $3T_{2g}$ (535–516, 444–427, and 211–198 cm^{-1}), and E_g (277–274 cm^{-1}) (Fernandes et al., 2014; Jacintho et al., 2009; Pereira et al., 2012; Shebanova and Lazor, 2003). These results confirm the nature of the iron oxide cores indicated by XRD. Additional phonon modes around 774–766, 623–619, 497 and 351–347 cm^{-1} can be detected (marked with asterisks in Fig. S2), due to nanoscale quantum size effects resulting from the reduced size of the MNPs relative to the excitation radiation wavelength. This phenomenon causes a breach of the moment conservation law and, consequently, the appearance of additional active phonon modes in Raman spectra (Chourpa et al., 2005; Degiorgi et al., 1987; Jacintho et al., 2009). Nevertheless, a slight oxidation of the Fe_3O_4 surface to maghemite may also be present (De Faria et al., 1997; Jacintho et al., 2009; Pereira et al., 2012).

The Raman spectrum of the Fe_3O_4@Au-SAM 0:1, which was the material with the best electrochemical performance (see below), is depicted in Fig. 3B. The expanded view in the range of 3000–2600 cm^{-1} (inset) evidenced the presence of broad bands in the 3000–2800 cm^{-1} region, corresponding to CH_2 symmetric and asymmetric stretching modes from the MCHac compound and/or to CH_3 symmetric and asymmetric stretching modes from ethanol, the solvent of the thiols (Bazylewski et al., 2017; Socrates, 2004). The bands related to C–H and C–C bending vibrations arising from ethanol and MCHac compound are visible at about 1442 and 1424 cm^{-1} and 1296–1100 cm^{-1}, respectively (Bazylewski et al., 2017). Moreover, an intense peak is observed at 1040 cm^{-1} associated with C–C–O stretching vibrations from ethanol and MCHac, as well as an additional band in the 960–860 cm^{-1} region assigned to C–S–H bending vibrations from MCHac (Socrates, 2004). The peaks located around 660–630 cm^{-1} are assigned to a group of C–S stretching modes from MCHac compound, the one centered at 458 cm^{-1} is associated with C–O bending vibrations, and the peak centered at 587 cm^{-1} corresponds to O–H out-of-plane bending vibrations. These last two modes of vibration arising from ethanol and MCHac compound (Bazylewski et al., 2017; Socrates, 2004). On the other hand, the interaction of MCHac with the gold surface *via* a gold–sulphur bond was observed through the band at 273 cm^{-1}, which correspond to the Au–S stretching mode (Holze, 2015; Joo et al., 2000).

Since sulphur is a relevant element of the functionalized samples (Fe_3O_4@Au-SAM), and in order to confirm the presence of the SAMs, the S content was determined by chemical analysis for the sample that provided the best electrochemical performance (Fe_3O_4@Au-SAM 0:1). The result obtained was 0.31 mmol/g, which confirms that the SAM incorporation was successful, being in agreement with the data of Raman spectroscopy, where the presence of sulphur was detected through the presence of the peaks at 660–630 cm^{-1} and 273 cm^{-1} from C–S and Au–S stretching vibration modes, respectively.

3.2. Optimization of genoassay

The approach used in this work is shown in Scheme 1. A SAM of alkanethiols is formed on the Au shell (Scheme 1A) and the aminated capture probe (CP) is linked through carbodiimide chemistry (Scheme 1B, step 1). A sandwich assay is performed with a FITC-tagged signaling probe (FITC-SP) to allow enzymatic labelling (steps 2 and 3). MNPs are deposited on SPCE with the help of a magnet and the chronoamperometric detection was carried out using TMB + H_2O_2 as a substrate of peroxidase (steps 4 and 5).

To obtain a good analytical performance, some operating conditions were studied using the event-specific target and then applied to the

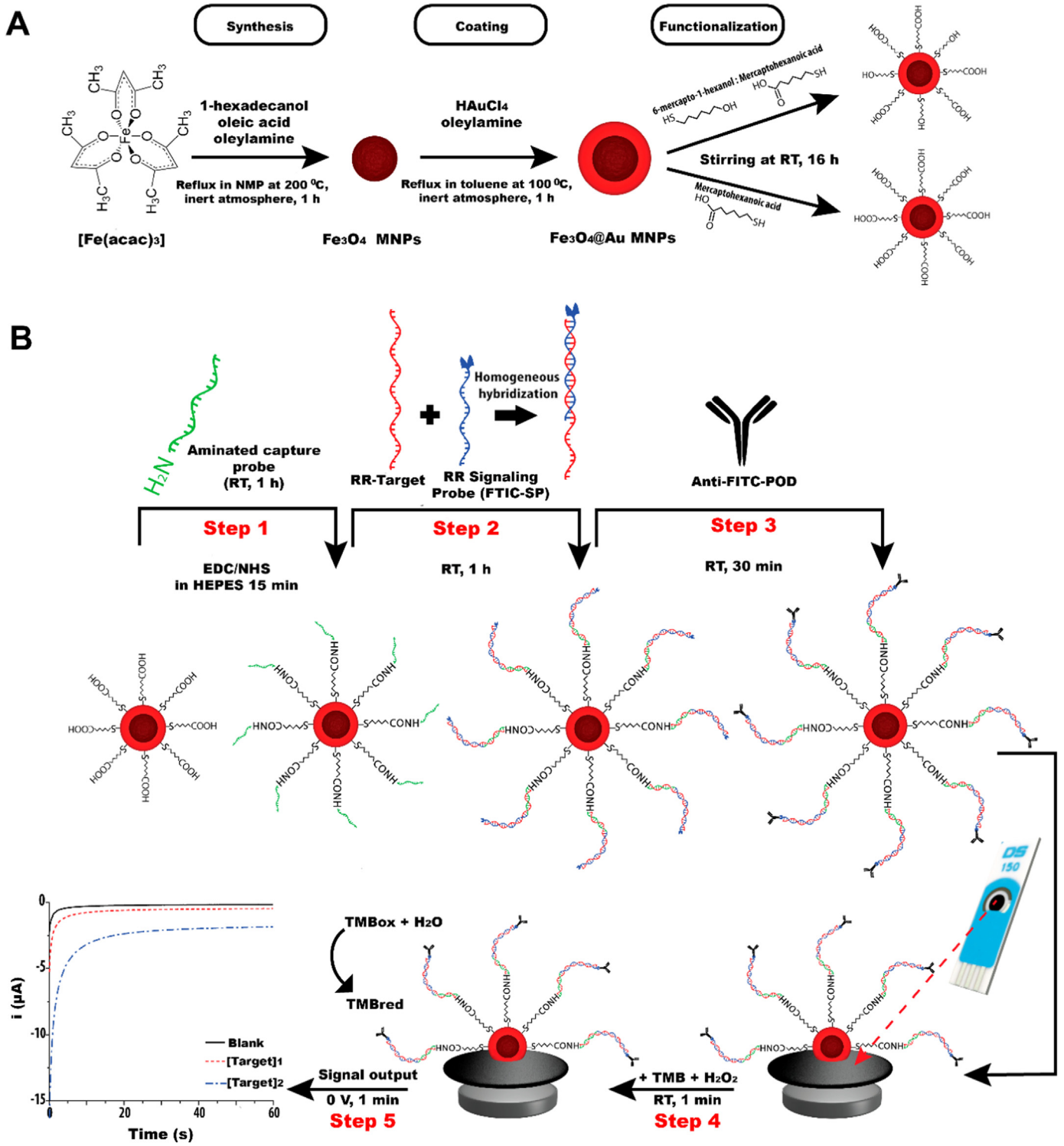

Scheme 1. Schematic illustration of the electrochemical magnetogenoassay design to detect GTS 40-3-2 soybean event: (A) Core-shell Fe_3O_4@Au MNPs synthesis, and surface functionalization with MCH and/or MCHac; and (B) magnetogenoassay procedure divided into four steps: (1) immobilization of the CP to the surface of Fe_3O_4@Au MNPs through the EDC/NHS reaction; (2) homogeneous hybridization between the signaling probe and the target sequence, and subsequent heterogeneous hybridization reaction with capture probe; (3) enzymatic labelling with Fab-enzyme conjugate; and (4) electrochemical detection of TMB_{ox} at the electrode surface by chronoamperometry. The approach for lectin detection was identical, only changing the DNA sequences.

taxon-specific assay.

Blocking agents such as bovine serum albumin (BSA) added to the heterogeneous hybridization solution usually help to reduce the blank signals, improving the signal to blank (S/B) ratio by preventing non-specific interactions. In our case, the presence of BSA (2.5% in 2× SSPE buffer) decreased both the blank and specific signals, leading to a very limited effect on the S/B ratio (5.4 ± 0.1 and 5.14 ± 0.05 with and without BSA for 2 nM of target, respectively) (Fig. 4A). Since both the S/B and the reproducibility were not improved, BSA was not included in the following assays.

The hybridization in solution between the SP and the target can be carried out at room temperature or using a thermal shock (5 min at

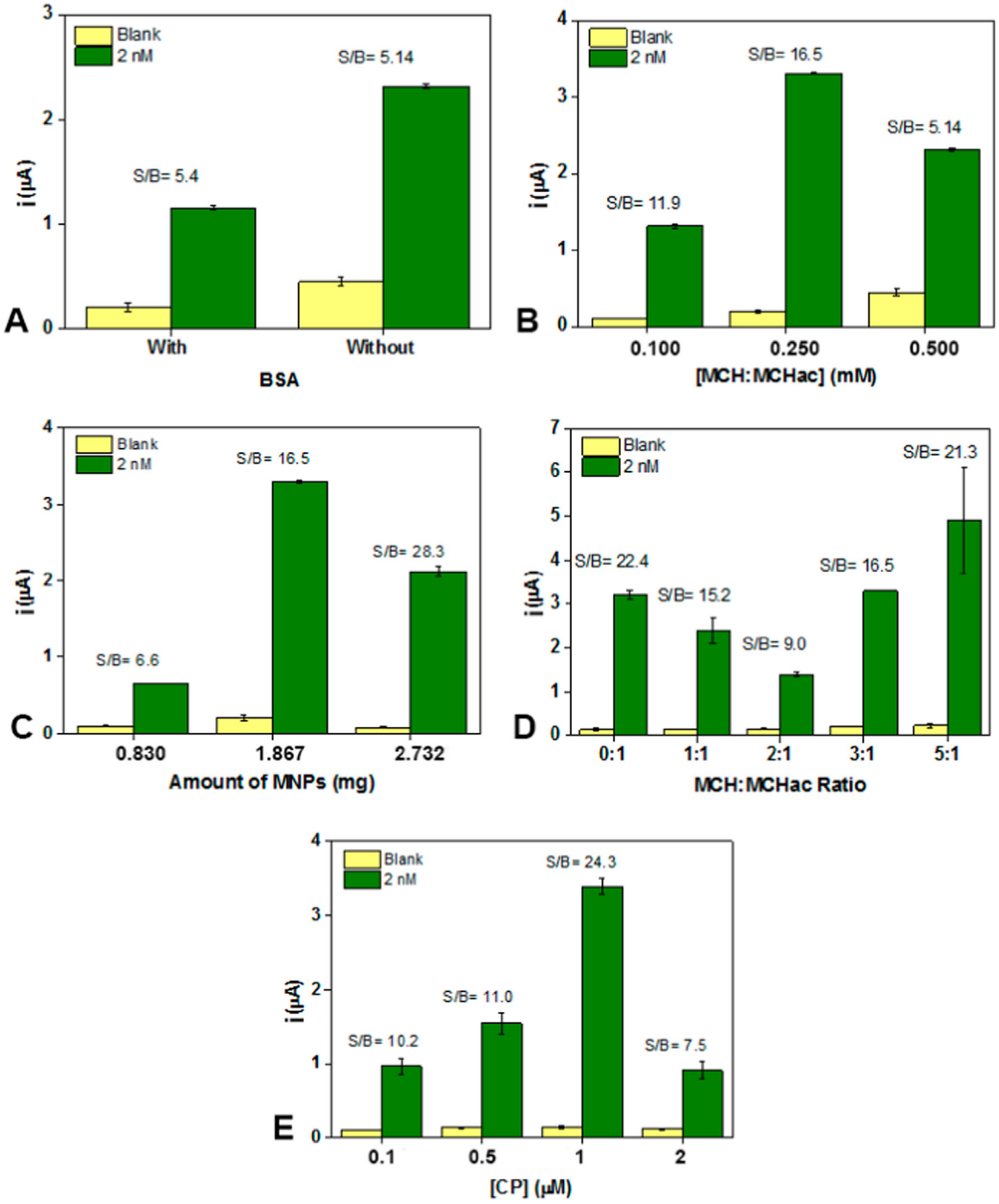

Fig. 4. Effect of BSA used in the hybridization step (A), total thiol concentration (B), amount of MNPs (C), thiols ratio used in the SAM formation step (D), and CP concentration employed to construct the biolayer (E) on the current intensity in the absence (yellow columns), and in the presence of 2 nM DNA RR target (green columns). S/B ratios are also indicated. Geometric working electrode area = 0.063 cm^2. Experimental conditions were 1.867- of MNPs (except in C); SAM 3:1 except in E were 0:1 was used and in D; MCH:MCHac 0.250 mM except in A were 0.500 mM was used and in B; 1 μM CP except in E and SP 0.25 μM in all cases. BSA was not used except in A.

98 °C and 5 min in an ice bath). It is expected that probes with strong secondary structures require full opening at high temperatures to completely hybridize with the short SP. In the present case, the thermal shock was beneficial although the theoretical Gibbs energy of the target is not too high, −5.85 kcal/mol (at 20 °C and $[Na^+]$ = 0.3 M). The S/B value increased from 5.14 to 16.5 when 2 nM of target was tested.

Optimization of the composition of the sensing biolayer is of paramount importance because it determines the amount and distribution of carboxylic groups available for covalent linkage of aminated DNA capture probe (CP). Interestingly, the two-step coupling reaction must be performed without washing steps to hinder hydrolysis of the activated intermediate. Indeed, the current intensity dramatically increased from 0.16 to 2.0 μA for 2 nM of target using a SAM formed from a 3:1 mixture of 0.250 M MCH:MCHac and 1 μM of CP, which is compatible with a much higher yield of the chemical coupling. Direct immobilization of thiolated DNA is very common but a relatively long spacer is recommended to avoid steric inaccessibility and lead to a layer with a greater free volume as compared with DNA directly bound to the

surface. Three critical parameters were studied, namely the influence of concentration and ratio of thiols (mercaptohexanol and mercaptohexanoic acid) and the amount of MNPs. Fig. 4B shows the results obtained for three total concentrations of thiols assayed (0.100, 0.250, and 0.500 mM) mixed in a 3:1 ratio, revealing that the current intensity and the S/B ratio reach a maximum value at 0.250 mM. At 0.100 mM the amount of functional groups for DNA binding is insufficient. At 0.500 mM the decrease in the current reflects low accessibility to the incoming strand, which is due to the excess of carboxylic groups inadequately distributed for CP optimal separation that ensure high hybridization efficiency with the target. Using 0.250 mM total thiol concentration, the ratio of MNPs to the volume of thiols solution during the formation of SAM was proved to be a critical parameter. Three amounts of MNPs (0.820, 1.867, and 2.732 mg) were studied (Fig. 4C). Although the highest S/B ratio was obtained for 2.732 mg of MNPs, the reproducibility of the results was poorer and the net current intensity larger with 1.867 mg. It suggests that the homogeneity of the coverage is better for the middle amount of MNPs tested. Thus, 1.867 mg was chosen for subsequent experiments. After that, we studied the influence of five (MCH/MCHac) thiol ratios (Fig. 4D). The highest current response was reached with ratio 5:1, however the reproducibility was low owing to an irregular coating of the MNPs arisen from a low acid concentration. On the other hand, the results obtained with ratio 0:1 showed improved S/B ratio and reproducibility indicating that the concentration of MCHac used is sufficient to form a compact SAM avoiding nonspecific adsorptions that could affect hybridization. For this reason, the ratio 0:1 (pure SAM) was selected for the assays.

Not only the distribution of carboxylic groups but also the concentration of CP can affect the hybridization efficiency. Among the range tested, 0.1–2 μM, the best S/B ratio was achieved at 1 μM (Fig. 4E). There is a steady increase in the current up to 1 μM indicating an increase in the number of hybridization sites for the target. As expected, an excess of CP makes some of them unavailable for hybridization because of electrostatic repulsion. The optimum value is in good agreement with previous approaches using pure SAMs of carboxylic acids (Miranda-Castro et al., 2017). In general, low μM concentrations of DNA probes yield a coverage of about 1–3 × 10^{12} molecules/cm^2 (Barroso et al., 2015; Campuzano et al., 2011), a middle packed layer well-suited for hybridization (Ricci et al., 2007). In spherical surfaces, an order of magnitude higher coverage has been reported for 10 nm AuNPs directly modified with thiolated 25-mer DNA (Hill et al., 2009). This means that the maximum amount of oligonucleotides per NPs expected is about 68. Lower amounts of CP are required when generating direct ternary monolayers (Barroso et al., 2015; Wu et al., 2010) or when aromatic thiols are used as a diluent (Miranda-Castro et al., 2017). The optimized conditions are summarized in Table S2.

3.3. Analytical performance of genoassay

The genoassay response at different concentrations for both RR event and lectin were registered under the optimized conditions (Fig. S3) and the correlation between the chronoamperometric current and the concentration was established (Fig. 5A). The calibration curves depict a linear relationship in the range of 0.10–10 nM and 0.10–5.0 nM for RR and lectin, respectively. The linear regression equation for the RR genoassay was i (μA) = 0.84 (± 0.01) [RR] (nM) + 0.011 (± 0.007) (r = 0.9995, n = 3) and for the lectin genoassay was i (μA) = 1.21 (± 0.03) [Lec] (nM) + 0.10 (± 0.01) (r = 0.9990, n = 3). The limits of detection (LOD) and limits of quantification (LOQ) were calculated as three times and ten times the standard deviation of the blank divided by the slope of the calibration plot, respectively. The obtained LODs were 0.02 nM and 0.05 nM for RR and Lec, respectively. In the case of RR, the LOQ was found to be 0.07 nM while for Lec, the LOQ was 0.1 nM.

The intra-day reproducibility was evaluated at 5 nM of GTS 40-3-2

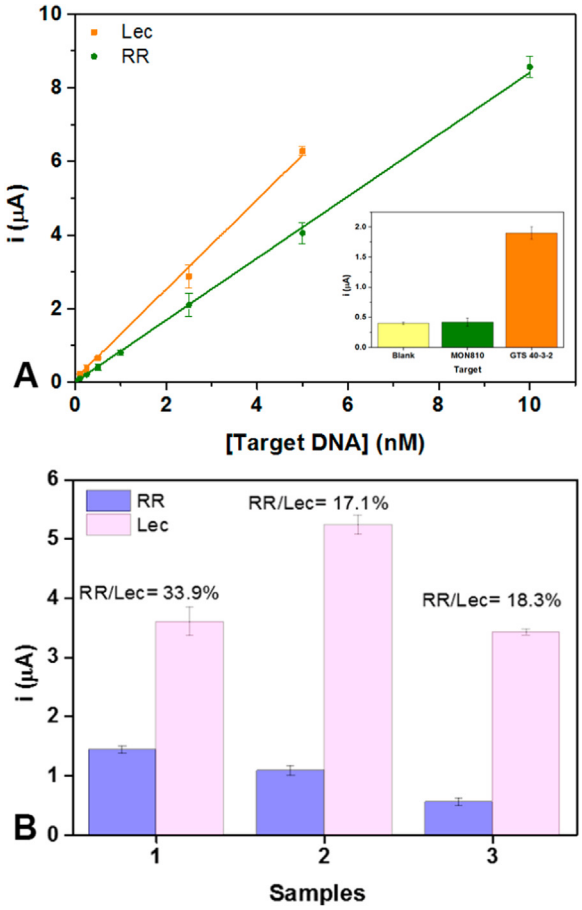

Fig. 5. (A) Calibration plots for RR soybean and *lectin* gene targets. Inset: current intensity for the blank experiment and for non-complementary (MON810) and target (GTS 40-3-2) DNA sequences at a concentration of 2.5 nM. Error bars represent the standard deviation from the mean of three independent measurements. (B) Analytical signals obtained after dilution of event-specific (1:20) and reference (1:50) amplified DNA of three real samples with the corresponding genoassays. The percentage of RR estimated in each sample is also indicated for each real sample. Geometric working electrode area = 0.063 cm^2.

and lectin target DNA. The maximum relative standard deviation (RSD) was 3.9% and 2.1% for the transgenic and reference target, respectively, indicating a high precision for both genoassays. Additionally, the inter-day reproducibility was also estimated to be 5.4% and 6.3% for RR and Lec, respectively, showing a good assay-to-assay reproducibility especially when considering the platform is a synthesized nanomaterial chemically modified. Probably, the high stability and excellent dispersion of Fe_3O_4@Au MNPs are the main characteristics for the good reproducibility obtained for both genoassays, as already seen in a previously work (Freitas et al., 2016). Nonetheless, in this approach the LOD was improved and the linear range extended probably due to a careful optimization of the CP concentration and the monolayer that includes only a thiol, which favors reproducibility and homogeneity. The nanoscale properties of these MNPs have put forward an alternative viable to magnetic microbeads used in a similar approach (Manzanares-Palenzuela et al., 2015) in terms of reproducibility though the sensitivity remains unmatched because of the low background currents obtained. In fact, other chronoamperometric genosensors performed directly on non-nanostructured Au electrodes reported a higher LOD of 225 pM (Liao et al., 2013). Alternative electrochemical techniques such as CV, DPV or SWV with different electroactive probes added after hybridization reached LOD ranging from 22.5 nM (Ren et al., 2005) to 0.290 pM (Sun et al., 2013). The latter employed reduced graphene

oxide as a platform for probe immobilization, which confirms that nanomaterials improve the analytical features in genoassays. The best detectabilities are achieved, however, by electrochemical impedance spectroscopy after amplification with an enzymatic reaction yielding an insoluble product (Lucarelli et al., 2005) or in combination with a variety of complex hybrid nanomaterials, which make the methods less amenable (Yang et al., 2009; Zhou et al., 2009). Optical methods such SPR or lateral flow devices do not improve the LOD reported with electrochemical transduction including this work; *e.g.* 2.5 nM (Giakoumaki et al., 2003) or 160 pM (Kalogianni et al., 2006).

A non-complementary sequence corresponding to a specific sequence of the maize MON810 transgenic event was chosen to study the selectivity. The results showed the current intensity near to the blank response, confirming the specificity of both genoassays (Fig. 5A inset).

3.4. Detection of GTS 40-3-2 in food samples

Finally, the usefulness of our approach was validated through the application to real samples. All DNA extractions were performed with a blank extraction and all PCR runs included positive and negative controls to ensure the absence of cross-contaminations or false positive results. For this purpose, the DNA was extracted and the quality of all obtained extracts was assessed by agarose gel electrophoresis and UV spectrophotometry. The qualitative PCR determined that all the samples contained amplifiable plant DNA (amplification of RUBISCO, as DNA quality control) and were positive to the endogenous gene, *lectin*. PCR amplification with event specific primers showed that all samples contains transgenic soybean. Amplicons without purification were subjected to the developed genoassay protocols in substitution of the synthetic oligonucleotide targets. The GMO percentage was calculated dividing the value of the GMO-specific measurement with the value of the *lectin* (in ng), using the regression equations and the molar mass of each sequence as established the legislation (Arugula et al., 2013). As expected, higher current intensities were obtained for the lectin assay, the endogenous gene of soybean. RR soybean is present in all samples, and the quantitative analysis indicates that the RR content ranges from 12 ± 2 to 34 ± 2% (Fig. 5B). These results prove the ability of the proposed methodology to be used as an alternative for quantification of GTS 40-3-2 event in feed and food samples.

4. Conclusions

In this work, the quantification of GMOs in percentage as legislation demands was successfully addressed by developing two electrochemical sandwich genoassays for RR soybean event, based on core-shell Fe_3O_4@Au MNPs functionalized with a pure layer of mercaptohexanoic acid. The Fe_3O_4 MNPs were successfully synthesized by thermal decomposition and coated with gold (Fe_3O_4@Au) by the chemical reduction method. The study of SAM composition revealed that 0.250 mM of MCHac was sufficient to avoid nonspecific adsorptions without addition of MCH nor BSA, showing that the use of a blocking agent is not necessary. The magnetogenoassays demonstrated good sensitivity, and reproducibility. Furthermore, the assays are selective, exhibit low detection limits (20 pM and 50 pM for event and taxon specific assay, respectively), and were successfully applied to real samples. To the best of our knowledge this is the second genoassay aimed at quantifying not only the transgenic event but also the reference gene to allow real quantification. Future genoassay developments must pursuit this objective in order to become a suitable low-cost, portable alternative to real-time PCR methods in decentralized analysis.

Acknowledgements

This work received financial support from the European Union (FEDER funds through COMPETE), National Funds (FCT, Fundação para a Ciência e a Tecnologia) through project UID/QUI/50006/2013 and Regional Funds (Principado de Asturias government through Project FC15-GRUPIN14-025), and cofinanced by FEDER funds. A.P. and M.F.B. are grateful to FCT grants SFRH/BD/97995/2013 and SFRH/BPD/78845/2011, financed by POPH–QREN–Tipologia 4.1–Formação Avançada, subsidized by Fundo Social Europeu and Ministério da Ciência, Tecnologia e Ensino Superior. C.P. thanks FCT for the FCT Investigator contract IF/01080/2015.

References

Arugula, M.A., Zhang, Y., Simonian, A.L., 2013. Anal. Chem. 86 (1), 119–129.
Barroso, M.F., Freitas, M., Oliveira, M.B.P., de-los-Santos-Álvarez, N., Lobo-Castañón, M.J., Delerue-Matos, C., 2015. Talanta 134, 158–164.
Bazylewski, P., Divigalpitiya, R., Fanchini, G., 2017. RSC Adv. 7 (5), 2964–2970.
Boisselier, E., Astruc, D., 2009. Chem. Soc. Rev. 38 (6), 1759–1782.
Campuzano, S., Kuralay, F., Lobo-Castañón, M.J., Bartošík, M., Vyavahare, K., Paleček, E., Haake, D.A., Wang, J., 2011. Biosens. Bioelectron. 26 (8), 3577–3583.
Chourpa, I., Douziech-Eyrolles, L., Ngaboni-Okassa, L., Fouquenet, J.-F., Cohen-Jonathan, S., Soucé, M., Marchais, H., Dubois, P., 2005. Analyst 130 (10), 1395–1403.
De Faria, D., Venâncio Silva, S., De Oliveira, M., 1997. J. Raman Spectrosc. 28 (11), 873–878.
Degiorgi, L., Blatter-Mörke, I., Wachter, P., 1987. Phys. Rev. B 35 (11), 5421.
Dinnebier, R.E., Billinge, S.J., 2008. Powder Diffraction: Theory and Practice, first ed. RCS Publishing, Cambridge, UK.
European Commission, 2003. Regulation (EC) No 1829:2003 of the European Parliament and of the Council of 22 September 2003 on Genetically Modified Food and Feed. L268.
Fernandes, C., Pereira, C., Guedes, A., Rebelo, S.L., Freire, C., 2014. Appl. Catal. A 486, 150–158.
Freitas, M., Sá Couto, M., Barroso, M.F., Pereira, C., de-los-Santos-Álvarez, N., Miranda-Ordieres, A.J., Lobo-Castañón, M.J., Delerue-Matos, C., 2016. ACS Sens. 1, 1044–1053.
Giakoumaki, E., Minunni, M., Tombelli, S., Tothill, I.E., Mascini, M., Bogani, P., Buiatti, M., 2003. Biosens. Bioelectron. 19 (4), 337–344.
Hill, H.D., Millstone, J.E., Banholzer, M.J., Mirkin, C.A., 2009. ACS Nano 3 (2), 418–424.
Holze, R., 2015. Phys. Chem. Chem. Phys. 17 (33), 21364–21372.
ISAAA, 2016. ISAAA Brief No. 52, ISAAA: Ithaca, NY.
Jacintho, G.V., Brolo, A.G., Corio, P., Suarez, P.A., Rubim, J.C., 2009. J. Phys. Chem. C 113 (18), 7684–7691.
Joo, S.W., Han, S.W., Kim, K., 2000. J. Phys. Chem. B 104 (26), 6218–6224.
Kalogianni, D.P., Koraki, T., Christopoulos, T.K., Ioannou, P.C., 2006. Biosens. Bioelectron. 21 (7), 1069–1076.
Kamle, S., Ali, S., 2013. Gene 522 (2), 123–132.
Kolen'ko, Y.V., Bañobre-López, M., Rodríguez-Abreu, C., Carbó-Argibay, E., Sailsman, A., Piñeiro-Redondo, Y., Cerqueira, M.F., Petrovykh, D.Y., Kovnir, K., Lebedev, O.I., 2014. J. Phys. Chem. C 118 (16), 8691–8701.
Liao, W.-C., Chuang, M.-C., Ho, J.-aA., 2013. Biosens. Bioelectron. 50, 414–420.
Lucarelli, F., Marrazza, G., Mascini, M., 2005. Biosens. Bioelectron. 20 (10), 2001–2009.
Manzanares-Palenzuela, C.L., de-los-Santos-Álvarez, N., Lobo-Castañón, M.J., López-Ruiz, B., 2015. Biosens. Bioelectron. 68, 259–265.
Miranda-Castro, R., Sánchez-Salcedo, R., Suárez-Álvarez, B., de-los-Santos-Álvarez, N., Miranda-Ordieres, A.J., Lobo-Castañón, M.J., 2017. Biosens. Bioelectron. 92, 162–170.
Moura-Melo, S., Miranda-Castro, R., de-los-Santos-Alvarez, N., Miranda-Ordieres, A.J., Dos Santos Junior, J.R., da Silva Fonseca, R.A., Lobo-Castañón, M.J, 2015. Anal. Chem. 87 (16), 8547-–88554.
Paleček, E., Fojta, M., 2007. Talanta 74 (3), 276–290.
Pereira, C., Pereira, A.M., Fernandes, C., Rocha, M., Mendes, R., Fernández-García, M.P., Guedes, A., Tavares, P.B., Grenèche, J.-M., Araújo, J.P., Freire, C., 2012. Chem. Mater. 24 (8), 1496—11504.
Plácido, A., Amaral, J., Costa, J., Fernandes, T., Oliveira, M., Delerue-Matos, C., Mafra, I., 2016. Regulation and Public Health, Waltham, MA, USA, pp. 119–131.
Ren, Y., Jiao, K., Xu, G., Sun, W., Gao, H., 2005. Electroanalysis 17 (23), 2182–2189.
Ricci, F., Lai, R.Y., Heeger, A.J., Plaxco, K.W., Sumner, J.J., 2007. Langmuir 23 (12), 6827–6834.
Robinson, I., Tung, L.D., Maenosono, S., Wälti, C., Thanh, N.T., 2010. Nanoscale 2 (12), 2624–2630.
Shebanova, O.N., Lazor, P., 2003. J. Solid State Chem. 174 (2), 424–430.
Socrates, G., 2004. Infrared and Raman Characteristic Group Frequencies: Tables and Charts, third ed. John Wiley & Sons, New York.
Sun, W., Zhang, Y., Hu, A., Lu, Y., Shi, F., Lei, B., Sun, Z., 2013. Electroanalysis 25 (6), 1417–1424.
Wang, L., Wang, L., Luo, J., Fan, Q., Suzuki, M., Suzuki, I.S., Engelhard, M.H., Lin, Y., Kim, N., Wang, J.Q., 2005. J. Phys. Chem. B 109 (46), 21593–21601.
Wang, Z., Wu, L., Wang, F., Jiang, Z., Shen, B., 2013. J. Mater. Chem. A 1 (34), 9746–9751.
Wu, J., Campuzano, S., Halford, C., Haake, D.A., Wang, J., 2010. Anal. Chem. 82 (21), 8830–8837.
Xu, Z., Hou, Y., Sun, S., 2007. J. Am. Chem. Soc. 129 (28), 8698–8699.
Yang, T., Zhou, N., Zhang, Y., Zhang, W., Jiao, K., Li, G., 2009. Biosens. Bioelectron. 24 (7), 2165–2170.
Zhou, N., Yang, T., Jiang, C., Du, M., Jiao, K., 2009. Talanta 77 (3), 1021–1026.